IVYSPRING INTERNATIONAL PUBLISHER

Theranostics

2017; 7(2): 329-343. doi: 10.7150/thno.17574

Research Paper

Tumor Stiffening, a Key Determinant of Tumor Progression, is Reversed by Nanomaterial-Induced Photothermal Therapy

Iris Marangon[1], Amanda A. K. Silva[1], Thomas Guilbert[2], Jelena Kolosnjaj-Tabi[1], Carmen Marchiol[2], Sharuja Natkhunarajah[2], Foucault Chamming's[3], Cécilia Ménard-Moyon[4], Alberto Bianco[4], Jean-Luc Gennisson[5], Gilles Renault[2], Florence Gazeau[1]✉

1. Laboratoire Matière et Systèmes Complexes (MSC), CNRS-UMR 7057, Université Paris Diderot, Sorbonne Paris Cité, 10 rue Alice Domon et Léonie Duquet, F-75205 Paris Cedex 13, France
2. Plateforme Imagerie, Institut Cochin, Inserm U1016-CNRS UMR8104-Université Paris Descartes, Sorbonne Paris Cité Paris, 22 rue Méchain, 75014 Paris France
3. PARCC, Inserm U970, Paris Cardiovascular Research Center-PARCC / Université Paris-Descartes, Sorbonne Paris Cité, 56 rue Leblanc, 75015, Paris, France
4. University of Strasbourg, CNRS, Immunopathology and Therapeutic Chemistry, UPR 3572, 67000 Strasbourg, France
5. Institut Langevin, CNRS-UMR 7587, 1 place Jussieu, 75205 Paris, France.

✉ Corresponding author: Florence GAZEAU, florence.gazeau@univ-paris-diderot.fr. Tel: +33 (0)1 57 27 62 03; Fax: +33 (0)1 57 27 62 11.

Received: 2016.09.14; Accepted: 2016.10.24; Published: 2017.01.01

Abstract

Tumor stiffening, stemming from aberrant production and organization of extracellular matrix (ECM), has been considered a predictive marker of tumor malignancy, non-invasively assessed by ultrasound shear wave elastography (SWE). Being more than a passive marker, tumor stiffening restricts the delivery of diagnostic and therapeutic agents to the tumor and *per se* could modulate cellular mechano-signaling, tissue inflammation and tumor progression. Current strategies to modify the tumor extracellular matrix are based on ECM-targeting chemical agents but also showed deleterious systemic effects.

On-demand excitable nanomaterials have shown their ability to perturb the tumor microenvironment in a spatiotemporal-controlled manner and synergistically with chemotherapy. Here, we investigated the evolution of tumor stiffness as well as tumor integrity and progression, under the effect of mild hyperthermia and thermal ablation generated by light-exposed multi-walled carbon nanotubes (MWCNTs) in an epidermoid carcinoma mouse xenograft. SWE was used for real-time mapping of the tumor stiffness, both during the two near infrared irradiation sessions and over the days after the treatment. We observed a transient and reversible stiffening of the tumor tissue during laser irradiation, which was lowered at the second session of mild hyperthermia or photoablation. In contrast, over the days following photothermal treatment, the treated tumors exhibited a significant softening together with volume reduction, whereas non-treated growing tumors showed an increase of tumor rigidity. The organization of the collagen matrix and the distribution of CNTs revealed a spatio-temporal correlation between the presence of nanoheaters and the damages on collagen and cells. This study highlights nanohyperthermia as a promising adjuvant strategy to reverse tumor stiffening and normalize the mechanical tumor environment.

Key words: photothermal therapy, carbon nanotubes, cancer, elastography, tumor microenvironment.

Introduction

Tissue mechanics is modified in tumor progression at both cell- and tissue-level. Current clinical techniques (elastography) interrogate tissue stiffness as a passive feature to detect cancer. In particular, ultrasound shear wave elastography (SWE) as well as magnetic resonance elastography

yield quantitative information capable of discerning benign versus malignant lesions, the latter being characterized by increased stiffness.[1, 2] Experimental evidences also suggest that tissue mechanics, *per se*, is a key modulator of tumor progression and clinical outcome. Analyses of human breast cancer of increasingly aggressive subtype revealed that cancer transformation is accompanied by a progressive increase in collagen deposition and a linearization and thickening of interstitial collagen. At the invasive region of the tumor, the stroma is the most heterogeneous and the stiffest while the number of infiltrating tumor-activated macrophages and TGF beta signaling are the highest. These observations suggest a tight relationship between extracellular matrix (ECM) remodelling and stiffening, cellular mechanosignaling, tissue inflammation and tumor aggression.[3] A causal relationship between ECM stiffening and the most aggressive cancer subtypes could provide a set of prognostic biomarkers. Although molecular mechanisms by which altered mechanics regulate tumor behavior remain unclear, a number of mechanosignaling pathways have been recently demonstrated. For example, inducing collagen crosslinking by lysyl oxidase stiffens the ECM, promotes focal adhesion by forcing integrin clustering, enhances PI3 kinase activity and induces the invasion of a premalignant epithelium.[4] Increased matrix stiffness also modulates the expression of tumor suppressor genes through a microRNA (miRNA)–mediated transcriptional circuit. In patient samples, the abundance of miRNA-18a was higher in breast tumor tissue than in normal tissue, and correlated with tumor stiffness, aggression and poor survival.[5] Such new mechanism orchestrated by a microRNA circuit is shown to mediate the physical effects of the microenvironment on tumor cell progression.[6]

The tumor microenvironment also mediates the response of solid tumors to chemo- and nanoparticle-based therapies. Aberrantly abundant and dense ECM, high interstitial pressure, chaotic vessel organization, enhanced solid stress are physical features that dramatically restrict the transport of cytotoxic therapeutic agents.[7-9] Such physical barriers directly contribute to decreased therapeutic efficacy and the emergence of drug resistance by creating drug-free sanctuaries. This is particularly true in pancreatic ductal adenocarcinoma characterized by an intense desmoplastic reaction which regulates interstitial transport of drugs.[10] Ablating the constituants of ECM with enzymatic and receptor-based means including collagenase, matrix metalloproteinases and angiotensin receptor blockers is part of the recent approaches being explored to render the tumor more profoundly vulnerable to chemotherapeutics and nanoparticles.[10-15]

Alternatively, physical strategies using electromagnetic or acoustical waves [e.g., radiofrequency ablation, high-intensity focused ultrasound (HIFU) or magnetic and photothermal therapy (PTT)] are increasingly explored. Particularly, nanoparticles that can be activated on demand at a distance through external electromagnetic fields offer a more localized control of heating in tumor environment. Among photoactivable nanostructures, both plasmonic metallic nanoantennae (mostly gold particles) and carbon-based absorbing nanomaterials [e.g. carbon nanotubes (CNTs) and graphene oxide] have shown great promises for tumor treatment via localized heating when exposed to near-infrared (NIR) light.[16] However, the multifaceted effects of nanoparticle-mediated hyperthermia on the tumor microenvironment remain elusive. Recent studies have mainly focused on the vascular barrier showing that local heating by nanoparticles could be exploited to increase the vascular permeability and spectacularly enhance the accumulation of molecular and nanosized (10-200 nm) agents into the tumor parenchyma.[17] However, this effect could be tempered by the acquisition of a vascular thermotolerance upon reexposure to NIR, which represents an important adaptation of tumors to heat.[18] Shifting the focus to the interstitial barriers, we recently demonstrated that mild hyperthermia generated by magnetic nanocubes under an alternating magnetic field had a local effect on the organization of collagen fibers that improved nanoparticle penetration in the tumor after repeated treatment and potentiate the delivery and efficacy of doxorubicin.[19] Gold nanorods heated to ablative temperature (>50°C) also induced significant collagen remodeling.[20] Hence, the ECM could be an important target of nanohyperthermia with still-underestimated effects on drug transport and normalization of tumor stiffness. Insight on how nanomaterial-mediated heating induces remodeling of ECM and how tumor stiffness might be modulated by hyperthermia would guide the development of oncologic approaches that use thermal energy generated at the nanoscale.

Here, we explored the effects of local heating induced by multi-walled CNTs (MWCNTs) on epidermoid carcinoma microenvironment with the goal to relate the tumor stiffness evolution with tumor progression. Two conditions of heating were investigated by tuning NIR irradiation power: mild hyperthermia (43°C for 15 min) and thermal ablation (52°C for 3 min) representing thermal doses differing by three orders of magnitude.[21] SWE imaging was used for real-time mapping of the tumor stiffness,

both during the two NIR irradiation sessions and over the days after the treatment, in parallel to the tumor volume monitoring. Ultrasound-based elastography was recently evaluated to monitor tumor stiffening associated to malignant progression and histopathological features.[22-24] This non-invasive technique also proved useful for quantitative monitoring of thermal ablation by radiofrequency or HIFU in liver and heart[25, 26] and to determine the elasticity threshold predictive of coagulation necrosis.[27, 28] SWE was used in our study for the first time to get insight into nanothermotherapy effects on the tumor environment.

Simultaneous monitoring of the tumor temperature by infrared imaging thermometry and of the tumor stiffness by SWE revealed a transient and reversible stiffening of the tumor tissue during laser irradiation, which was lowered at the second session of mild hyperthermia or photoablation. In contrast, over the days following PTT, the treated tumors exhibited a significant reduction of their stiffest area together with volume reduction, whereas non-treated tumors showed an increase of tumor stiffness which correlates with tumor growth. Such normalization of the tumor tissue elasticity is indicative of the response to PTT. At the microscopic level, the organization of the collagen matrix[29] and the distribution of CNTs was assessed using two-photon excitation fluorescence microscopy (TPEF) and second harmonic generation microscopy (SHG) demonstrating a spatial correlation between the presence of the nanoheaters and the damages on collagen. Thus, we propose that CNT-induced thermal damages and subsequent remodeling of the tumor environment represent a promising adjuvant strategy to reverse tumor stiffening and normalize the tumor microenvironment.

Results

PTT was performed in mice bearing epidermoid carcinoma flank tumors after intratumoral administration of CNTs and exposition to 808 nm laser (**Figure 1**). Temperature monitoring indicated a step increase in the recorded tumor surface temperature as laser was turned on and an instantaneous drop as laser was turned off. The tumor temperature was increased to 52°C for 3 min for thermal ablation, and to 43°C for 15 min for mild hyperthermia treatment. During both treatments, the heart rate and, to a larger extent the respiratory rate, were slightly enhanced, as well as the rectal temperature (Supporting information **Figure S1**). In tumors non-injected with CNTs, unspecific heating of 2°C and 1.4°C was observed keeping laser settings of thermal ablation and mild hyperthermia, respectively.

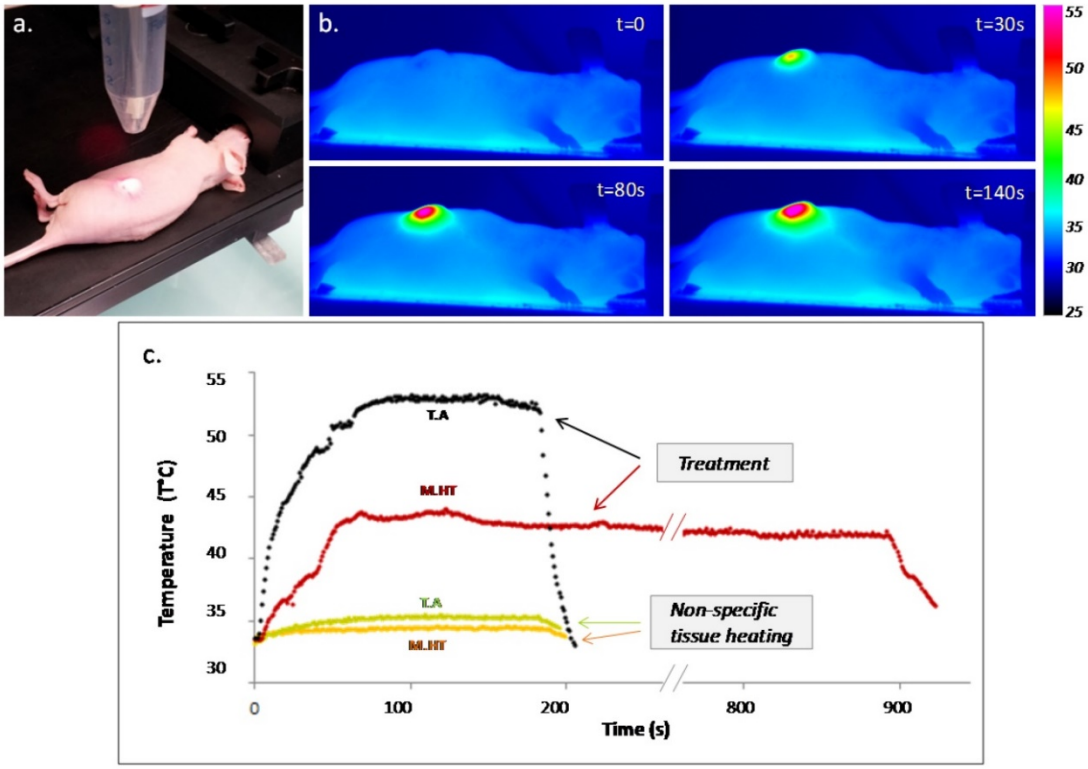

Figure 1: Photothermal treatment mediated by CNTs. (a) Picture of a near-infrared irradiation (808 nm, 1 W/cm²) set-up *in vivo* with laser beam focusing on the tumor area. (b) Thermographic infrared pictures of a mouse under laser exposure during thermal ablation at four time points; right scale representing the color code for surface temperature. (c) Surface temperature plot as a function of the time for thermal ablation (T.A., in black – 3 min) and mild hyperthermia (M.H.T., in red – 15 min) and the related non-specific tissue heating for non-injected tumors for 3 min.

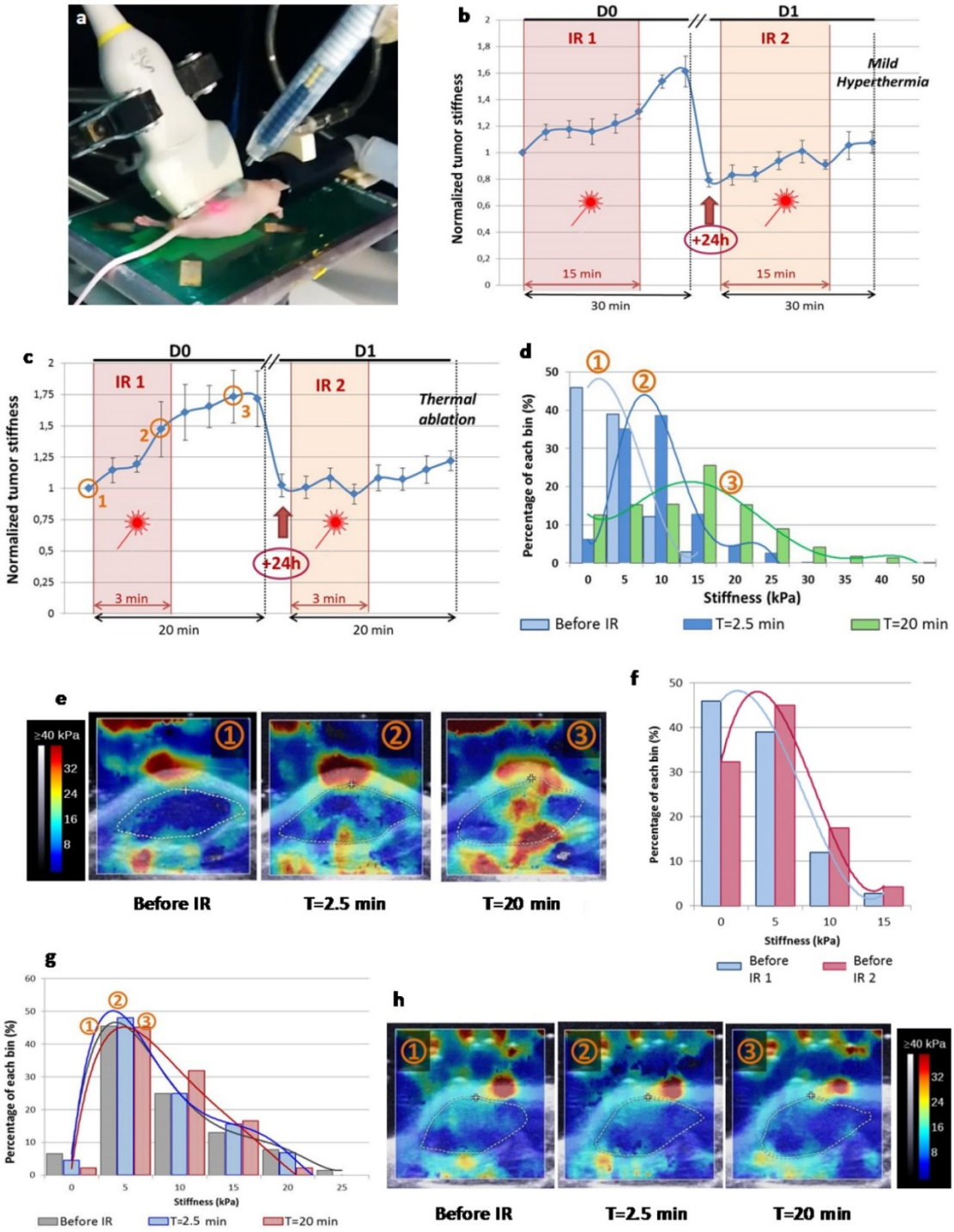

Figure 2: Real-time SWE mapping and quantification of tumor stiffness during thermal therapy. (a) Picture of the experimental set-up with near-infrared irradiation (IR) (808 nm, 1-2 W/cm²) with simultaneous SWE *in vivo*. (b) Normalized mean tumor stiffness as a function of the time featuring laser exposure windows for mild hyperthermia group (n=6). (c) Normalized mean tumor stiffness plot as a function of the time featuring laser exposure windows for thermal ablation group (n=12). (d) Histogram illustrating the shift of the stiffness distribution for the tumor represented in (e), at three time points before, during and after the first irradiation of thermal ablation treatment (IR1). (e) SWE color stiffness mapping at three time points before, during and after the first irradiation of thermal ablation. (f) Histogram of the stiffness distribution of the same tumor before the first irradiation of the thermal ablation treatment (IR1) and before the second irradiation (IR2) showing the reversibility of laser-induced stiffening during IR1. (g) Histogram of the stiffness distribution for the control non-injected tumor represented in (h) at three time points before, during and after IR1 at the laser set-up corresponding to thermal ablation. (h) SWE color stiffness mapping at three time points for a control tumor before, during and after IR1.

PTT Induces a Transient and Reversible Stiffening of Treated Tumors

To evaluate the impact of CNT-mediated PTT on tumor stiffness during laser exposure time lapse, we performed SWE real-time monitoring (**Figure 2**). SWE mapping of tumor stiffness showed an acute effect during both thermal ablation and mild hyperthermia procedures. A transient and reversible stiffening of tumor tissue was observed for both, although thermal

ablation induced a more pronounced effect (50% increase in tumor stiffness versus 30% for mild hyperthermia). The stiffness continued to be monitored in the minutes following the treatment time lapse showing that it still increased. Interestingly, the tumor stiffness returned to its starting value 24 h after the first laser exposure for thermal ablation condition or even to a reduced level in the case of mild hyperthermia. PTT-induced tumor stiffening was also observed in the course of the second laser exposure, but to a lesser extent when compared to the first treatment (10% stiffness increment). There was no stiffness increment for control tumors non-injected with CNTs and irradiated at the laser set-up of thermal ablation or mild hyperthermia considering the time points before and after irradiation.

PTT Inhibits Tumor Growth and Stabilizes Tumor Stiffness: Towards a Marker of Therapeutic Response

Tumor growth was followed longitudinally by daily measurement of tumor dimensions (**Figure 3**a-b). There was a steep rise in tumor growth for control animals with an almost 12-fold increase in tumor volume from days 0 to 10. Conversely, mild hyperthermia and thermal ablation inhibited tumor growth and induced tumor regression as tumor volume decreased by 2-fold considering equivalent time points.

In addition to tumor growth, SWE was used for mapping and quantifying tumor stiffness at several time points (**Figure 4**a-c). Interestingly, tumor stiffness increased with time for control group while it remained stable for both thermal ablation and mild hyperthermia treated groups. As it can be visualized in SWE maps, tumor stiffening onset was observed for control at day 4 with the appearance of regions above 30 kPa. These high stiffness zones were found to spread at day 6 extending nearly to the totality of the tumor at day 9. Stiffness remained constant within the tumor zone over time for treated groups. No significant difference was observed when comparing tumor stiffness for treated and control groups at day 2 and day 4. However, tumor stiffness markedly differed for control and treated animals at days 6 and 9.

As a function of a tumor volume decrease or increase following thermal therapy, treated tumors were classified into responsive and non-responsive, respectively. The percentage of intratumoral area featuring very high rigidity (above 40 kPa) was compared for these two subsets as well as for control (Figure 4d). At an early time point (day 2), there was no significant difference between these three groups. However the percentage of intratumoral area featuring very high rigidity (above 40 kPa) decreased for the treatment-responsive group only, from day 6 to 9. At day 9, this parameter was significantly different between the group responsive to treatment and the refractory one. It demonstrates that a reduction of the intratumoral area featuring very high rigidity was correlated to tumor regression. Therefore, this parameter may be considered as a marker of therapeutic outcome providing information on how tumors respond to thermal treatment.

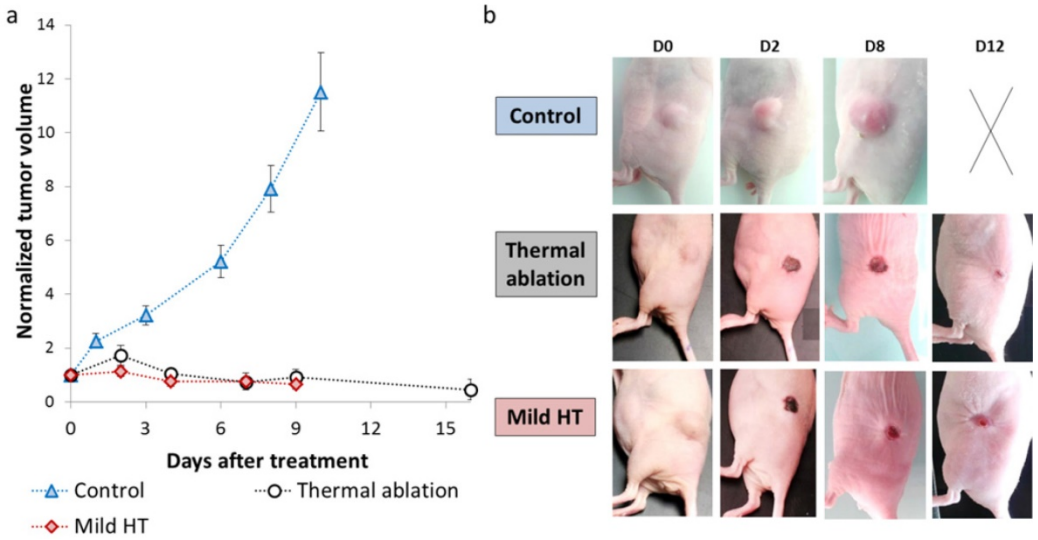

Figure 3: Photothermal therapy effect on tumor growth. (a) Tumor volume plot as a function of the time for control (n=14), mild hyperthermia (n=6) and thermal ablation (n=14) groups. Control group comprises non-CNT injected non-irradiated tumors (n=6) and non-CNT injected tumors irradiated with laser fluence used for mild hyperthermia (n=4) and thermal ablation (n=4). (b) Representative pictures of tumor growth evolution for control, mild hyperthermia and thermal ablation groups (The panel with the cross represents a sacrificed mouse whose tumor mass achieved ethical limit).

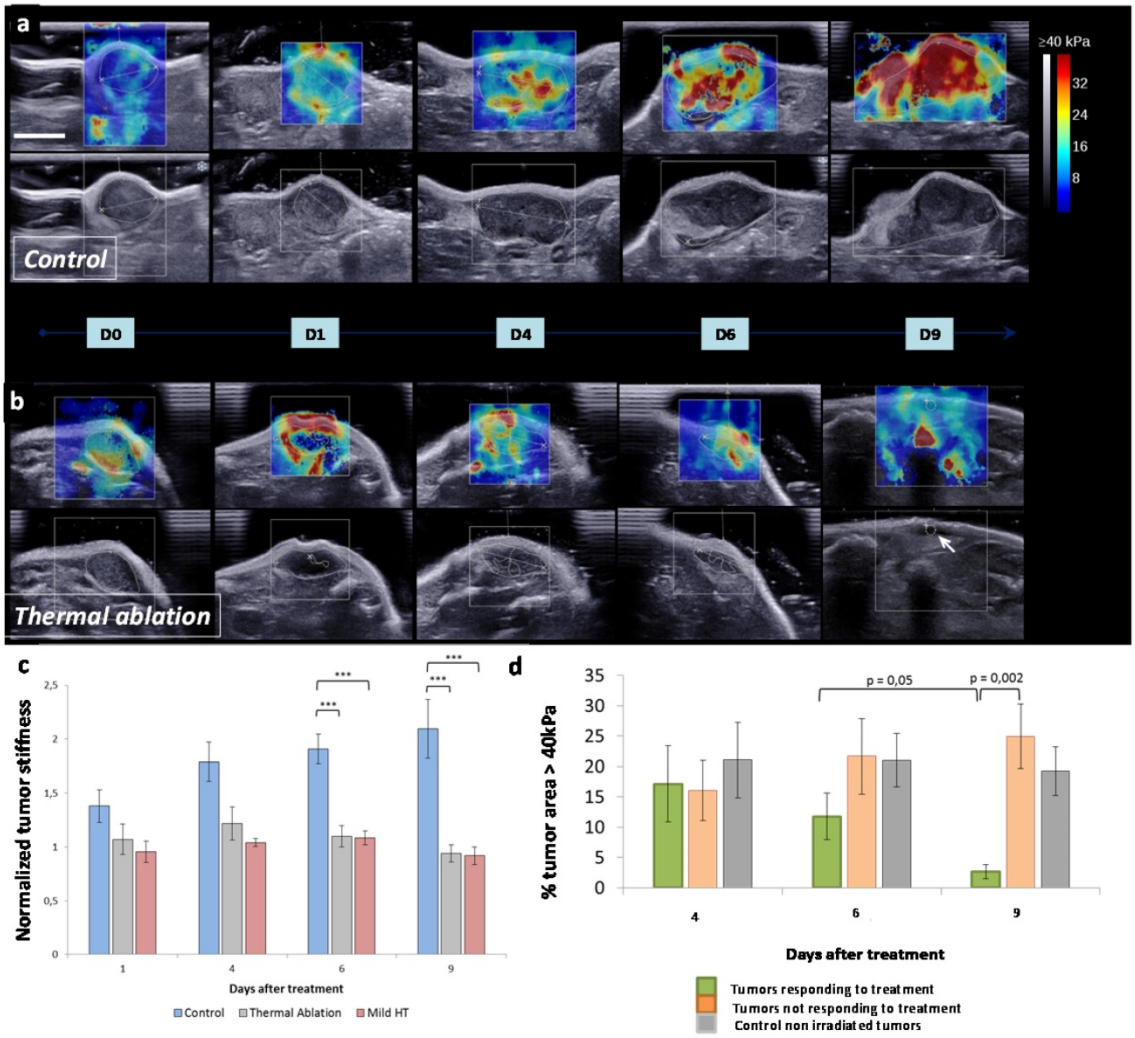

Figure 4: Evolution of the tumor stiffness following treatment. SWE color maps of stiffness (range 0-40 kPa) with corresponding B-mode view in the transverse plane of control (a) and treated (b) tumor over 9 days. Color scale is the same for all measurements and scale bar corresponds to 5 mm. The white arrow (D9, treated) indicates the location of the residual tumor. (c) Quantitative analysis of the normalized mean tumor stiffness for 9 days for control tumors (n=8) and CNT-injected tumors treated either by thermal ablation (n=12) or mild hyperthermia (n=6). The mean stiffness was normalized to the baseline value at day 0 before the first irradiation for each tumor (***p≤0.0004). (d) Quantitative analysis of the percentage of intratumoral area above the threshold of 40 kPa for three time points after treatment. Tumors treated by thermal ablation or mild hyperthermia were classified into treatment responsive (n=9) and non-responsive (n=7), as a function of the tumor volume decrease or increase following thermal therapy, respectively (**p=0.05 and ***p=0.002).

PTT is Associated with Immune Cell Infiltration while Inducing Hemorrhagic Necrosis

Histological HES or Masson's trichrome staining revealed that control tumors (CNT-injected but not laser irradiated and non-injected but irradiated) typically presented a necrotic core and a well-vascularized layer of viable tumor cells surrounded by a collagen-rich stroma (**Figure S2** and **Figure 5**a-b). Histological analyses of tumor slices from PTT-treated groups evidenced extended necrosis (Figure 5c-g and **Figure S3**). Thermal ablation and mild hyperthermia induced an immediate impact on tumor tissue as hemorrhagic necrosis was observed at 1h time point (Figure 5c-g). Both thermal treatments were found to extend necrosis into tumor tissues and inflammatory infiltration was often observed in the necrotic tissue. CNTs were evidenced as black spots (Figure 5a-b-c-e). They were visualized embedded into necrosis zones associated with immune cell infiltration for PTT-treated tumors or in viable cell layers of injected non-irradiated tumors. CNTs were also observed in the collagen-rich ECM of treated tumors or of injected non-irradiated tumors (Figure S3 and Figure 5a-b). At the microscopic level, TEM observations of CNT-injected non irradiated tumors showed disseminated CNTs along collagen fibrils as well as CNT aggregates in the extracellular space (**Figure S4**). Following thermal ablation (**Figure S5**) and mild hyperthermia (**Figure S6**), CNT aggregates were surrounded by highly damaged ECM and cells, while collagen matrix distant from CNTs remained intact.

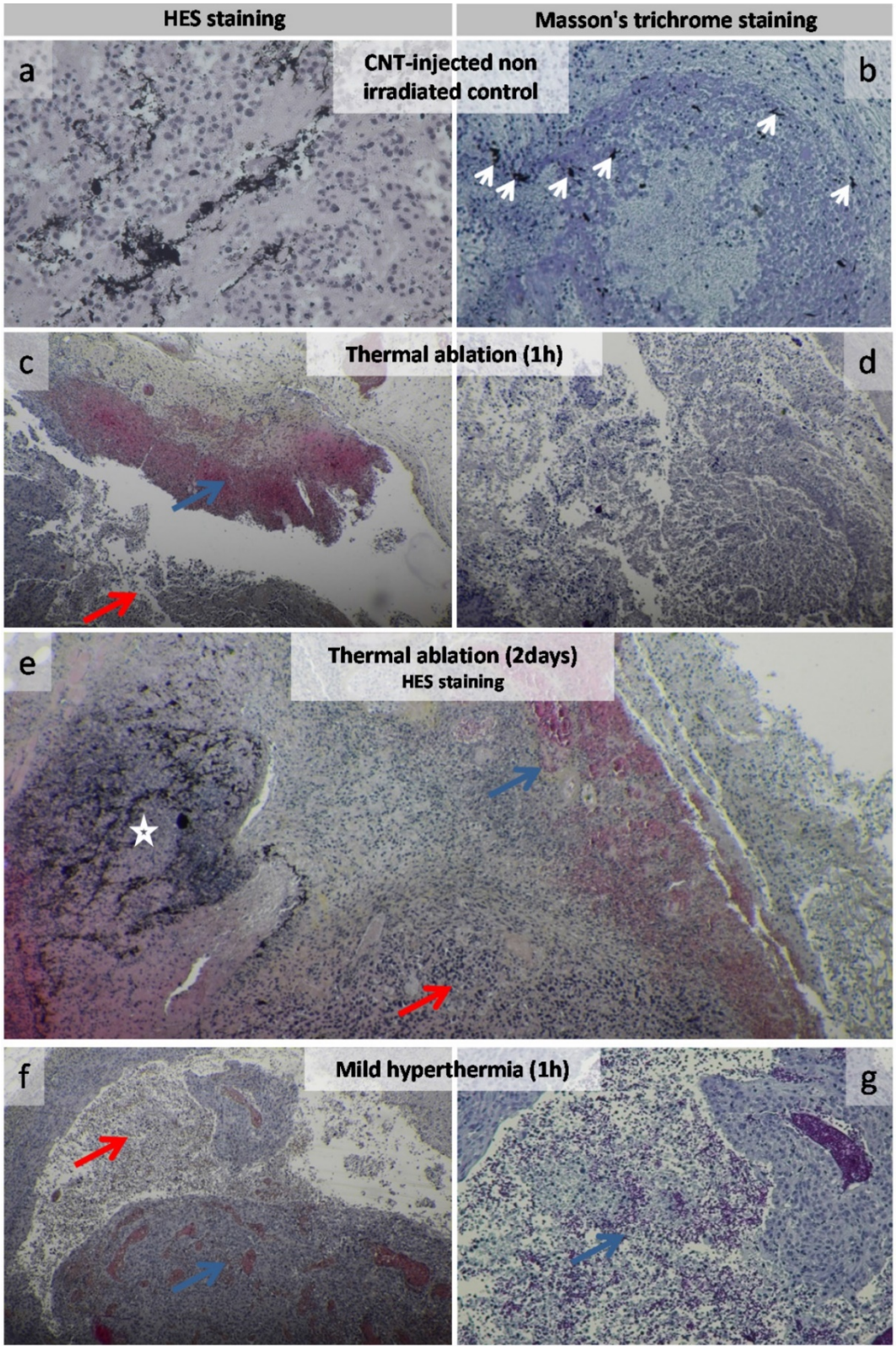

Figure 5: Histological analysis of CNT-injected non-irradiated control, thermal ablation and mild hyperthermia groups. Control group of CNT-injected non-irradiated tumor (a-b). High magnification view of tumor cell mass featured carbon nanotubes among tumor cells (a). Carbon nanotubes were visualized as dark spots near collagen fibers (left white arrows) and in the tumor mass featuring inflammatory cells (center and right white arrows) (b). Tumor 1 h following thermal ablation (c-d) featuring an extended necrotic zone (red arrow) including hemorrhagic necrosis (blue arrow) (c). Necrotic tissue at higher magnification (d). Tumor 2 days following thermal ablation featuring an extended necrotic zone (red arrow) including hemorrhagic necrosis (blue arrow) with a zone featuring a large amount of carbon nanotubes (white star) (e). Tumor 1 h following mild hyperthermia (f-g) featuring an extended necrotic zone (red arrow) including hemorrhagic necrosis (blue arrow) (f). Hemorrhagic necrotic tissue (blue arrow) at higher magnification (g).

PTT Induces Collagen Destructuration in the Tumor Site

PTT effect on tumor stiffness may be related to the cytotoxic action on cells reducing cell density in the tumor mass, but also on the ECM. Thus SHG microscopy was used to image collagen fibers as well as CNTs *ex vivo* using optical conditions preserving the integrity of the analyzed sample slices (**Figure S7**). Tuning the pulsed laser at 810 nm allowed imaging type I and III collagen fibers through SHG as well as CNTs owing to their two-photon cross-section absorption in the entire visible spectrum. In contrast, by changing the excitation to 850 nm wavelength, only CNTs were detected. The signal of collagen fibers was thus isolated by subtracting 850 nm and 810 nm images.

Intact collagen fibers were observed for control tumors. For the injected groups, CNTs were also visualized as bright spots both at 810 and 850 nm excitation and nearby intact collagen fibers at 810 nm. However, collagen fibers were not visualized nearby CNTs of injected and irradiated tumors at 30-min and 1 day post-irradiation, indicating that CNT-mediated PTT could act on tumor ECM and induce destructuration of collagen fibers (**Figure 6**a).

In order to quantitatively appraise the co-localization of CNTs and of collagen destructuration, a Pearson's correlation coefficient was calculated considering the same region of interest from images acquired at 810 and 850 nm (Figure 6b). Collagen fibers being destructurated, the detected image at 810 nm matched the one at 850 nm for CNT-injected irradiated groups. Indeed Pearson's correlation coefficient was significantly different following thermal ablation and mild hyperthermia at 30 min and 1 day time points (Pearson's coefficient of about 0.8) compared to CNT-injected non-irradiated control tumors (0.5).

PTT-induced cell damages were also evaluated in tumor slices by TPEF microscopy (**Figure 7**). Without laser irradiation, the tissue preserved its integrity both in the presence or absence of CNTs. Following laser exposure, tissue damage was observed exclusively in the presence of CNTs, the zones devoid of CNTs preserving their integrity. As represented in Figure 7 c-d, a left-shift of the distribution of cell autofluorescence levels was observed following PTT indicating tissue damage in comparison to all three control conditions. A statistically significant nearly 2-fold decrease in the average autofluorescence cell signal was induced by PTT indicating extended cell damage.

Second Harmonic Generation to Induce and Image *In Situ* CNT-mediated PPT Damages in Real Time

For the above tissue analyses, TPEF/SHG laser exposure parameters were set in order to enable image acquisition without inducing artefactual destructuration of collagen and tissue destruction during analysis. In a different approach aiming to investigate in real time the CNT-induced PTT effects on tissue integrity at the microscopic level, we deliberately shifted to a regimen imputing a higher laser power into tissue slices and exciting the CNTs present in the analyzed tissue. We thus conceived simultaneous PTT and dual CNT/collagen imaging under SHG in real time. For this *in situ* experiment, CNTs were first injected in fresh sheep tendon, used as a model type 1 collagen-rich tissue. Experiments were also conducted on tumor tissue slices.

Figure S7 shows that CNT excitation upon 810 nm laser exposure at 40 mW induced an immediate and complete destruction of surrounding collagen fibers both in sheep tendon and tumor tissue. Indeed, collagen fibers initially colocalized with CNTs were no more detected after excitation when imaged with standard acquisition condition. Conversely, collagen fibers remained intact after excitation under the same conditions in zones devoid of CNTs. This evidenced that CNT-mediated PTT was indeed able to locally damage ECM via the destructuration of collagen fibers, confirming a causality effect. In addition to collagen denaturation, cell damage observed as dark areas in TPEF autofluorescence imaging was evidenced only in the presence of CNTs and following excitation. Conversely no cell damage was observed in the presence of CNTs under standard acquisition settings, confirming real-time cell destruction in response to CNT-mediated PTT.

Discussion

In the context of thermal treatment of tumors, the prediction of the multiscale heat-induced effects remains challenging. Particularly, the use of remotely activated nanomediators for local hyperthermia has been documented with focus on tumor growth and vascular effects, but much less is known on the remodeling effect on the tumor microenvironment. The present study aimed (1) to quantify in real time the changes of elasticity in epidermoid tumor during, and shortly after, two sessions of laser irradiation, (2) to follow-up elasticity variation and tumor growth ensuing the treatment, (3) to compare mild hyperthermia and photoablative treatment regimens, and (4) to characterize the direct damages of irradiated CNTs on ECM and cells.

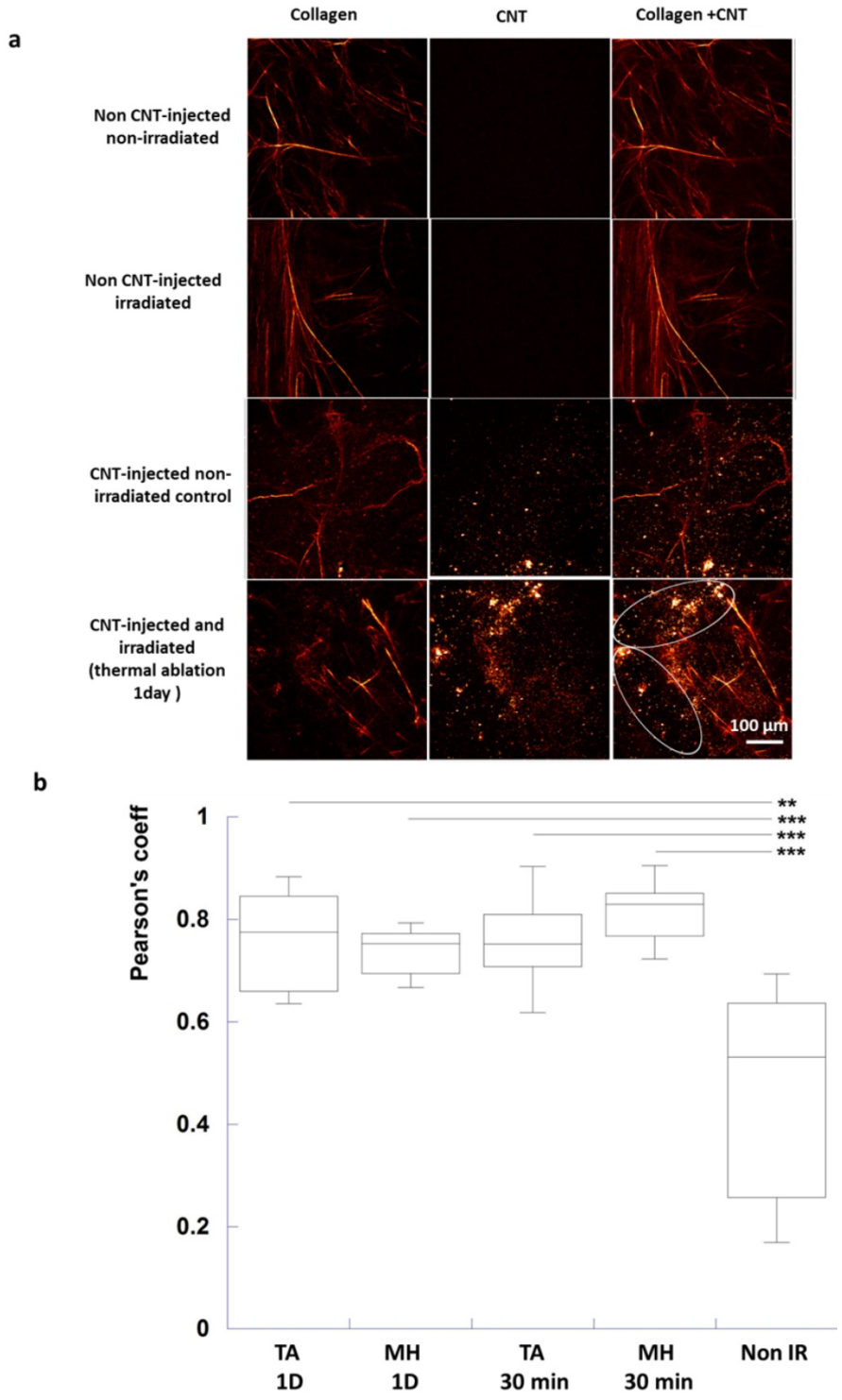

Figure 6: Collagen destructuration analysis by SHG in tumor slices in response to CNT-mediated PTT (a) Images of only collagen fibers were obtained by substracting the 850 nm excitation images to 810 nm ones. Images of only CNTs were acquired at 850 nm excitation wavelength. Images of both collagen and CNTs were obtained at 810 nm excitation wavelength. Intact collagen fibers were observed for the non CNT-injected non-irradiated control, the non CNT-injected irradiated control as well as for the CNT-injected non-irradiated control (first, second and third lines). For the latter, CNTs were visualized as bright spots (third line). For the CNT-injected and irradiated group (thermal ablation condition, 1 day time point in the fourth line), few intact collagen fibers were observed in zones devoid of CNTs while destructurated collagen fibers were visualized nearby CNTs (circled region). (b) Pearson's coefficient demonstrating the correlation between CNTs and collagen destructuration (n=12 slices from 3 different tumors for each condition, TA (MH) 1D: thermal ablation (respectively, mild hyperthermia) at day 1 post-irradiation, TA (MH) 30 min: thermal ablation (respectively, mild hyperthermia) 30 min post-irradiation).

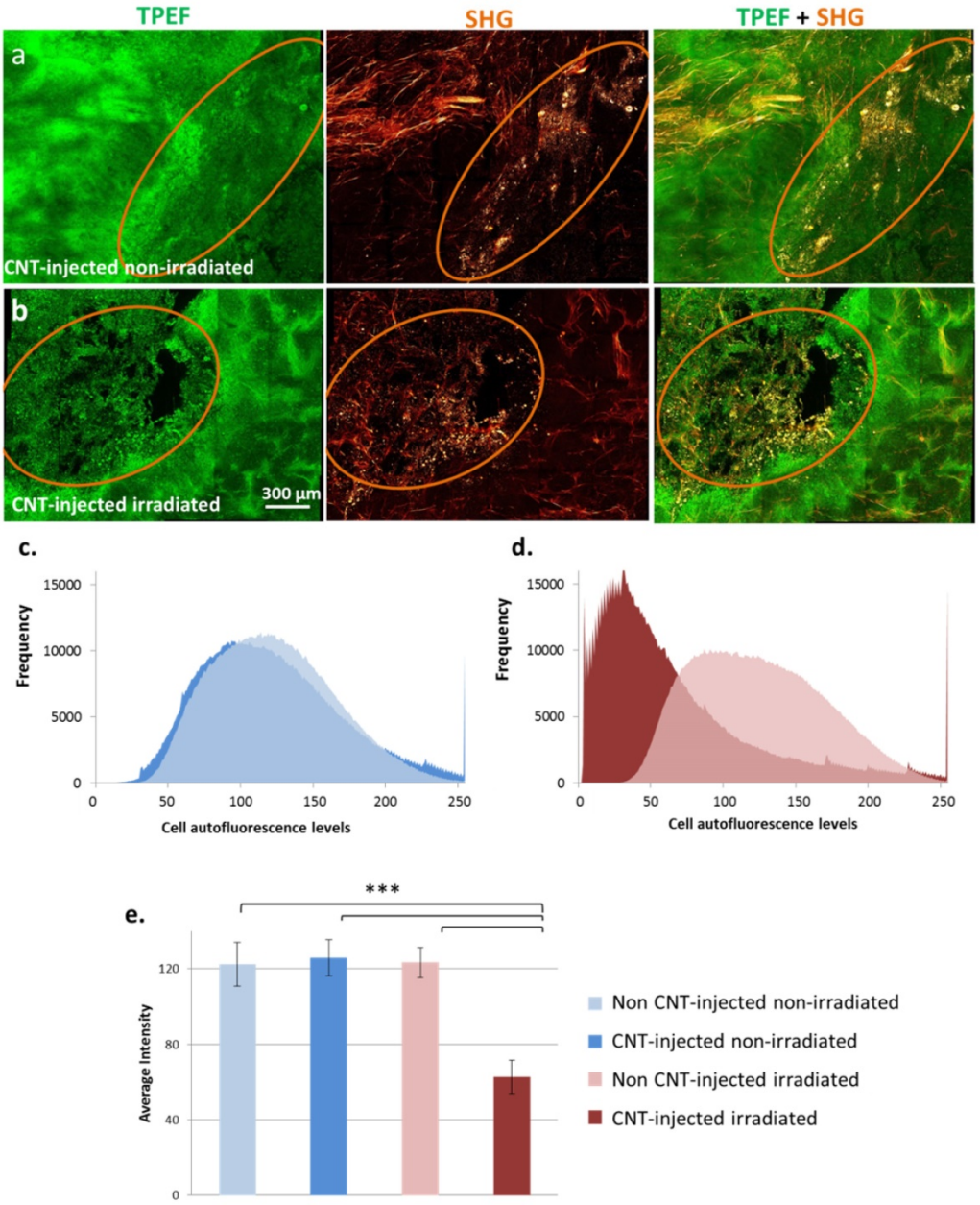

Figure 7: Cell damage evaluation by TPEF and SHG microscopy in response to CNT-mediated PTT in tumor slices. Each image is a reconstitution of 6×5 stitched pictures viewed in volume with the software Imaris BitPlan (8 steps of 15 µm). Circled regions indicate the presence of CNTs. Without laser irradiation, the integrity of the tissue was observed both in the presence or absence of CNTs (a) for CNT-injected non-irradiated control group. Under laser exposure, tissue damage correlated with the presence of CNTs while the tissue preserved its integrity in the regions devoid of CNTs for CNT-injected and irradiated group (b). Distribution of cell autofluorescence levels in TPEF images of tumor slices from non CNT-injected non-irradiated and CNT-injected non-irradiated conditions (c) as well as non CNT-injected irradiated and CNT-injected irradiated (thermal ablation at day 1) conditions (d). A left-shift of cell autofluorescence levels was observed following PTT indicating cell damage in comparison to all three control conditions. Average intensity of cell autofluorescence in TPEF images of tumor slices from non CNT-injected non-irradiated; CNT-injected non-irradiated conditions; non CNT-injected irradiated and CNT-injected irradiated (thermal ablation at day 1) conditions (e). A statistically significant nearly 2-fold decrease in cell signal was induced by photothermal treatment indicating cell damage (n=12 slices from 3 different tumors for each condition).

Previous studies have illustrated the role of heat stress mediated by photoresponsive nanoparticles on cell viability, cell metabolism, thermally activated drug delivery and radio- and chemosensitization at the cellular level.[30-33] However, regardless of the administration route, most nanoparticles do not attain the neoplastic cells because they are blocked in their diffusion or convection by disorganized blood and lymphatic vascular network, dense fibrous matrix, and off-target uptake by immune cells.[13, 34, 35] Consequently, the tumor stroma represents a new target for tumor treatment.[36] Nanohyperthermia was demonstrated to improve drug transport and tumor accumulation due to an increase of blood flow and interstitial extravasation.[17, 18] It is now well appreciated that the dense collagen matrix of tumor ECM also dramatically reduces the penetration and efficacy of drugs and nanotherapeutics.[13, 29] Losartan,

a clinically approved angiotensin II receptor antagonist was shown to inhibit collagen I production and improve drug/nanoparticle diffusion into tumors.[11] Other strategies proposed anti-ECM antibody to target collagen and achieve sustained release of proteins in the collagen network.[37] Regarding nanoparticle-based therapy, magnetic nanocubes were found embedded along the collagen fibers of epidermoid A431 tumor tissue eliciting structural change of the collagen network upon local heating, which favored further penetration of the nanoparticles and drug.[19] Gold nanorods accumulated near collagen fibrils *in vitro* were shown to denaturate the quarternary structure of collagen in response to NIR irradiation.[20,29] In the present work, we have demonstrated the local ablation of collagen fibers colocalizing with CNTs irradiated with NIR light. TPEF/SHG microscopies were successful in localizing both the collagen fibers and CNTs. In sheep tendon injected with CNTs, *in situ* laser scanning under the microscope induced thermal ablation of collagen (assessed by the disappearence of SHG signal related to collagen fibrils) exclusively in the region where CNTs were present. Adjacent CNT-free region showed intact collagen fibrils after laser scanning. The spatial selectivity of photothermal ablation of collagen could be estimated to a distance of about 10 µm around the CNT-rich zone. Similar laser scanning on tumor slices *ex vivo* allowed to demonstrate the selective denaturation of both the collagen and the cellularized tissue in the region of CNT accumulation. Due to highly efficient light-to-heat conversion by CNTs, collagen fibers gain enough energy to experience an irreversible transformation from an helical-ordered state to a random like structure, subsequently loosing their SHG signal, and cellular stuctures (including the neoplastic cells) are simultaneously ablated. Such real-time and *in situ* observations of CNT-dependent irradiation damages helped us to interpret the histological pattern of the different groups of tumors before and after treatment. In particular, the laser-induced destructuration of ECM and hemorrhagic necrosis were spatially correlated with the distribution of CNTs in the treated groups without differences between mild hyperthermia and thermal ablation conditions.

As the elastic properties of biological tissues are related to structural organizations at the molecular, cellular and tissular levels, tissue stiffness is expected to vary with thermal damages and protein denaturation.[38]

In this study, we took advantage of the real-time and quantitative capabilities of SWE to investigate for the first time the relationship between *in vivo* stiffness changes and temperature-controlled nanohyperthermia treatments. Despite the large heterogeneity of the stiffness pattern between the different tumors, the normalization of the mean stiffness value by its baseline value before the treatment enabled to provide statistically significant evolution over time during and after treatment. Significant differences were also evidenced between the treated and non-treated groups.

Importantly, stiffness monitoring revealed a two-stage process with contrasted evolution differentiating the acute response to the laser irradiation and the delayed effects on the days post-treatment. During the course of laser treatment and in the following 15 min cooling phase, a nearly two-fold increase of the tumor stiffness was observed both for mild hyperthermia and thermal ablation (+60% versus +75%, respectively). Interestingly, the stiffness was still increasing during the cooling phase, in line with a previous work using MR elastography to follow laser ablation of hepatic tumors.[39] This suggested that the tissue underwent a photo-induced denaturation process. However, more surprinsingly, the stiffness retrieved its initial value or a slightly lower value (-20%) on the day after the first treatment of thermal ablation and mild hyperthermia, respectively. The second treatment on day 2 induced a much lower stiffness increase in comparison to the first treatment (<+20%). The temporal reversibility of the photo-induced stiffness enhancement in the tumor is an important unexpected result in comparison to previous works aiming to characterize the thermal dependence of tissue stiffness. These studies determined a well-defined starting point of stiffening in muscle *ex vivo* and *in vivo* with a sharp slope rupture for temperature above 57°C and this change was particularly useful for non-invasive assessment of the spatial extention of thermal-induced necrotic lesions.[27, 28] For example, HIFU and radiofrequency ablated regions exhibited three to four times stiffer value in the post-treatment lesions, attributed to protein denaturation and tissue coagulative necrosis.[25, 26] However, the delayed response of the tissue mechanics to the thermal treatment was not explored. Here, we have shown a clear reversion of the acute heat-induced stiffening one day after the treatment. Moreover, a second hyperthermia treatment was not able to induce acute stiffening. Additionally the tumor stiffness tends to diminish over days after treatment in parallel to the tumor volume regression. These findings indicate a dynamic remodeling of the tumor tissue, which slackens following thermal ablation of ECM and cell structures. This second phase of tissue response corresponds to a diminution of the stiffest areas of the tumor, in contrast to the non-treated tumors which

show a stiffness enhancement. Moreover, the change of tumor stiffness correlates with tumor volume evolution parallely in treated and untreated tumors. Modification of tumor elasticity and heterogeneity was correlated with response to treatment. In good responders, elasticity and elasticity heterogeneity diminished. This suggests that the tumor elasticity evolution, non-invasively assessed by SWE, could be a prognosis marker of the tumor response to the photothermal treatment. The nanoparticle-mediated thermal damages deeply remodel the tumor microenvironment and consistently achieve objective tumor responses.

Another stricking results is that similar patterns of reversible stiffening (acute response) and delayed softening (delayed response) were found for mild hyperthermia and photoablation (although the short term kinetics were expectedly different). This result is in apparent contradiction with the concept of thermal dose established by Sapareto and Dewey to assess time-temperature dependent 50% necrosis on cells.[21] Cumulative equivalent minutes at 43°C (CEM43) is the accepted metric for thermal dose assessment that correlates well with the severity of thermal damage in a variety of tissues.[40] Moreover, a relationship between the thermal dose and the tissue stiffness evolution was also found.[28] Here, the thermal dose estimated from temperature measurement at the surface of the tumor, differed by three orders of magnitude between mild hyperthermia and photoablation conditions, but yet the elasticity variations in the tumor tissue were similar. This suggests that the apparent thermal dose is not appropriate to assess the effects of heat produced locally and from the inside by the accumulated CNTs, which may attain much higher temperatures at the microscopic scale. We can conclude from the similar effect of the mild hyperthermia and photoablation on the tumor stiffness and regression, that the energy deposition at the microscopic level of the mild hyperthermia condition is sufficient to achieve tumor response while diminishing off-target heat effects. This effect could be easily achieved even when lower dose of nanoheaters could penetrate the tumor after an intravenous injection. Here intratumoral administration of MWCNTs was prefered in order to modulate the heating regime by use of laser power and compare mild hyperthermia with thermal ablation.

In conclusion, photothermal therapy mediated by CNTs was found to normalize the aberrant stiffening of the tumor stroma, which is associated to tumor progression. Through a local denaturation of adjacent tissue and particularly on collagen fibers, nanomaterial-generated heat stress induce a remodeling and softening of the tumor microenvironment concomitant to tumor regression. SWE elastography imaging proved useful for tracking spatio-temporal biomechanical changes that occurred during nanoparticle-mediated hyperthermia and along the response of the tumor to the treatment. As the stiffening of the ECM is implicated in malignant transformation and also drives tumor invasion and metastasis, tumor softening could also represent a mechanical cue for tumor regression. Furthermore nanoparticle-induced ablation of the ECM physical barrier that currently limits the delivery of chemotherapeutics has the potential to enhance the efficacy of current treatments.

Materials and methods

Animal model and cell lines. All animal experiments were performed in agreement with institutional animal use and care regulations after approval by the local Ethics Committee. Eight-week-old female nude NMRI mice (40 animals provided by Janvier, France and weighing 30 ± 2 g) were housed in polypropylene cages and were provided with food and water *ad libitum*. The animals were allowed to acclimate to the facility for at least one week before being used in the experiments.

A431 human epidermoid carcinoma cells were cultured as adherent cells in complete RPMI culture medium supplemented with 10% (v/v) fetal bovine serum and 100 U/mL penicillin streptomycin at 37°C in 5% CO_2.

Each mouse was subcutaneously injected on both flanks with 1.5×10^6 A431 cells resuspended in a volume of 100 µL of physiological saline per inoculum. When the tumor volume attained 60-70 mm^3 (about 20 days after the injection of A431 cells), tumors were considered ready for treatment. Throughout the experiment, tumor volumes were measured on a daily basis and calculated from the formula $V=(D\times d^2)/2$, where D is the longest diameter and d the diameter perpendicular to D.

Photothermal therapy and temperature monitoring. Multi-walled CNTs (95% purity; batch 1240XH, 20-30 nm diameter, 0.5-2 µm length) were purchased from Nanostructured and Amorphous Materials. To shorten the nanotubes and increase their water dispersibility, MWCNTs were first oxidized using a mixture of sulfuric acid and nitric acid in a water bath sonicator. Following this acidic treatment, the length of the nanotubes was reduced to ~ 400 nm. This treatment also introduced COOH groups, that are essential for high dispersibility, low toxicity, high cellular uptake, intravenous injectability and favorable pharmacokinetics for medical use as demonstrated earlier.[41] CNTs were sonicated for 10

min and dispersed in physiological saline at a concentration of 500 µg/mL. Electron microscopy characterization and determination of photothermal conversion efficiency of shortened and carboxylated MWCNTs have been detailed previously in reference [33].

During all PTT protocol steps, the mice were anesthetized with 2% isoflurane supplied in air mixture. The mice were first intratumorally injected with 50 µL of CNT suspension (500 µg/mL). About 5 min after injection, tumors were irradiated using a 808 nm diode laser featuring a fiber delivery system. The optical fiber was fixed so that the laser spot focused precisely on the tumor site. Two modalities of treatment were tested: the thermal ablation and the mild hyperthermia. The duration of treatment and the tumor temperature were 3 min at 52°C for thermal ablation and 15 min at 43°C for mild hyperthermia, respectively (corresponding to a laser output power at 0.3 W/cm^2 and 1 W/cm^2, respectively). The treatment was performed twice within an interval of 24 h. The time of the first treatment was considered time 0. The surface temperature on the mouse skin was mapped and monitored by a FLIR SC7000 infrared camera. All the acquisitions were processed by Altair software (FLIR Systems, Inc.).

Physiological parameters were acquired using the imaging station of the VEVO770 (Visualsonics, Toronto, Canada). This ultrasound device displays the physiological information gathered by the THM150 system (Indus Instruments, Houston, Texas, USA). Briefly, the animal under isoflurane anesthesia was positionned on the THM 150 heating pad, ECG contact Gel was applied on paws and each paw was maintained in contact with each electrode using adhesive. Body temperature was monitored using a rectal probe, enabling active control of the heating pad as well.

Shear wave elastography. Ultrasound tumor measurements were performed during laser irradiation and every 2 days during the entire follow-up of the tumor growth. Images were acquired with the ultrasound device Aixplorer (SuperSonic Imagine, Aix-en-Provence, France) using a 15-MHz superficial probe dedicated to research (256 elements, 0.125 µm pitch). During the measurements, the mice were anesthetized under isoflurane and their body temperature was maintained at physiological level using a heating plate. The tumors were covered with a layer of standard ultrasound gel before measurement. B-mode images were first acquired in order to delineate manually the region of interest (ROI) corresponding to the tumor contours. Secondly, SWE mode was performed using the penetration mode with a color scale ranging from 0 (transparent) to 40 kPa (red), arbitrarily chosen in the beginning of the study according to the expected stiffness values. The area, the diameter and a set of stiffness values (mean, minimum, maximum and standard deviation) were recorded for (i) the ROI as previously defined, and (ii) a subset region corresponding to the ROI saturated area (>40 kPa).

Histology. The tumors were excised and fixed in pH 7.4 phosphate-buffered 10% formalin. The tumors were dehydrated in graded solutions of ethanol and embedded in paraffin. Five micrometer tissue sections were stained by hematoxylin / eosin / Saffron (HES) and Masson's trichrome stain.

Transmission electron microscopy. The tumors were cut into 1 mm^3 pieces after excision and fixed with 2% glutaraldehyde in 0.1 M sodium cacodylate buffer, postfixed with 1% osmium tetroxide containing 1.5% potassium cyanoferrate, gradually dehydrated in ethanol, and embedded in Epon. Thin sections (70 nm) of selected zones were observed with Zeiss EM902 electron microscope operated at 80 keV (platform MIMA2, INRA, Jouy-en-Josas, France).

Two-photon-excited fluorescence and second harmonic generation microscopy. The images were obtained using an inverted stand Leica SP5 microscope (Leica Microsystems GmbH, Wetzlar, Germany) coupled to a femtosecond Ti:sapphire laser (Chameleon, Coherent, Saclay, France) tuned at a wavelength of 810 or 850 nm for all experiments. The laser beam was circularly polarized and a Leica Microsystems HCX IRAPO 25×/0.95 W objective was used. Second harmonic generation (SHG – collagen structures and CNTs) and two-photon-excited fluorescence (TPEF – autofluorescence and CNTs) signals were detected in epi-collection through a 405/15 and a 525/50 nm bandpass filters respectively, by NDD PMT detectors (Leica Microsystems) with a constant voltage supply, at constant laser excitation power, allowing direct comparison of TPEF and SHG intensity values. Isolated CNT signal was detected through the same filter with a 850 nm tuned laser to avoid the detection of second harmonic signal, with an increase of the laser power of 3% to offset the loss of power due to the wavelength change.

We first checked if the image acquisitions could be performed without damaging the analyzed tissue. In fact, SHG is a nonlinear imaging technique, as it uses a pulsed laser source with a very high peak power. Therefore, tissue destruction may be induced by the interaction between the pulsed laser and the CNTs present in the analyzed tissue depending on the set-up. For imaging purpose, standard acquisition conditions were 810 nm tuned pulsed laser, 20 mW at the exit of the 25× objective, NA0.95, W, Leica. This set-up induced no damage to tissues, even after 10

successive scans of the same region of interest in the presence or not of CNTs in the analyzed tissue.

In a different approach, we intentionally took advantage of the pulsed laser SHG microscopy to irradiate the CNTs present in the analyzed tissue in order to perform real-time PTT. For this purpose, the set-up was 810 nm laser exposures at 40 mW zoomed 18 times during 20 s.

Statistics. Data are presented as standard deviation from the mean or as standard error of the mean. The statistical significance of the differences between groups was assessed with the Mann-Whitney U Test using Xlstat software 2008 (Addinsoft, Paris, France). A minimum of 95% confidence level was considered significant.

Supplementary Material

Supplementary figures.
http://www.thno.org/v07p0329s1.pdf

Acknowledgement

This work was supported by the Agence Nationale de la Recherche (ANR) P2N program (NANOTHER project 2010-NANO-008-398 04) and through the LabEx SEAM (Science and Engineering for Advanced Materials and devices; ANR 11 LABX 086, ANR 11 IDEX 05 02)), by the Centre National de la Recherche Scientifique (CNRS) and by the International Center for Frontier Research in Chemistry (icFRC). *In vivo* imaging was performed at the Life Imaging Facility of Paris Descartes University (Plateforme Imageries du Vivant - PIV), partly supported by France Life Imaging (grant ANR-11-INBS-0006). We are grateful to S. Canevari for providing the tumor cells, to Christine Péchoux Longin and Sophie Chat for electron microscopy, to the Institut Cochin for histology, microscopy studies and animal facility and to Emmanuel Donnadieu, Pierre Bourdoncle and Olivier Clément for fruitful discussions.

Competing Interests

The authors have declared that no competing interest exists.

References

1. Berg WA, Cosgrove DO, Doré CJ, Schäfer FKW, Svensson WE, Hooley RJ, et al. Shear-wave Elastography Improves the Specificity of Breast US: The BE1 Multinational Study of 939 Masses. Radiology. 2012; 262: 435-49.
2. Pepin KM, Ehman RL, McGee KP. Magnetic resonance elastography (MRE) in cancer: Technique, analysis, and applications. Prog Nucl Magn Reson Spectrosc. 2015; 90–91: 32-48.
3. Acerbi I, Cassereau L, Dean I, Shi Q, Au A, Park C, et al. Human breast cancer invasion and aggression correlates with ECM stiffening and immune cell infiltration. Integr Biol. 2015; 7: 1120-34.
4. Levental KR, Yu H, Kass L, Lakins JN, Egeblad M, Erler JT, et al. Matrix Crosslinking Forces Tumor Progression by Enhancing Integrin Signaling. Cell. 2009; 139: 891-906.
5. Mouw JK, Yui Y, Damiano L, Bainer RO, Lakins JN, Acerbi I, et al. Tissue mechanics modulate microRNA-dependent PTEN expression to regulate malignant progression. Nat Med. 2014; 20: 360-7.
6. Seewaldt V. ECM stiffness paves the way for tumor cells. Nat Med. 2014; 20: 332-3.
7. Minchinton AI, Tannock IF. Drug penetration in solid tumours. Nat Rev Cancer 2006; 6: 583-92.
8. Jain RK, Stylianopoulos T. Delivering nanomedicine to solid tumors. Nat Rev Clin Oncol. 2010; 7: 653-64.
9. Torosean S, Flynn B, Axelsson J, Gunn J, Samkoe KS, Hasan T, et al. Nanoparticle uptake in tumors is mediated by the interplay of vascular and collagen density with interstitial pressure. Nanomed- Nanotechnol. 2012; 9: 151-8.
10. Provenzano PP, Cuevas C, Chang AE, Goel VK, Von Hoff DD, Hingorani SR. Enzymatic Targeting of the Stroma Ablates Physical Barriers to Treatment of Pancreatic Ductal Adenocarcinoma. Cancer Cell. 2012; 21: 418-29.
11. Diop-Frimpong B, Chauhan VP, Krane S, Boucher Y, Jain RK. Losartan inhibits collagen I synthesis and improves the distribution and efficacy of nanotherapeutics in tumors. Proc Natl Acad Sci U S A. 2011; 108: 2909-14.
12. Wong C, Stylianopoulos T, Cui J, Martin J, Chauhan VP, Jiang W, et al. Multistage nanoparticle delivery system for deep penetration into tumor tissue. Proc Natl Acad Sci U S A. 2011; 108: 2426-31.
13. Netti PA, Berk DA, Swartz MA, Grodzinsky AJ, Jain RK. Role of extracellular matrix assembly in interstitial transport in solid tumors. Cancer Res. 2000; 60: 2497-503.
14. Mok W, Boucher Y, Jain RK. Matrix metalloproteinases-1 and -8 improve the distribution and efficacy of an oncolytic virus. Cancer Res. 2007; 67: 10664-8.
15. Alexandrakis G, Brown EB, Tong RT, McKee TD, Campbell RB, Boucher Y, et al. Two-photon fluorescence correlation microscopy reveals the two-phase nature of transport in tumors. Nat Med. 2004; 10: 203-7.
16. Singh R, Torti SV. Carbon nanotubes in hyperthermia therapy. Adv Drug Deliver Rev. 2013; 65: 2045-60.
17. Sano K, Nakajima T, Choyke PL, Kobayashi H. Markedly Enhanced Permeability and Retention Effects Induced by Photo-immunotherapy of Tumors. ACS Nano. 2012; 7: 717-24.
18. Bagley AF, Scherz-Shouval R, Galie PA, Zhang AQ, Wyckoff J, Whitesell L, et al. Endothelial Thermotolerance Impairs Nanoparticle Transport in Tumors. Cancer Res. 2015; 75: 3255-67.
19. Kolosnjaj-Tabi J, Di Corato R, Lartigue L, Marangon I, Guardia P, Silva AKA, et al. Heat-Generating Iron Oxide Nanocubes: Subtle "Destructurators" of the Tumoral Microenvironment. ACS Nano. 2014; 8: 4268-83.
20. Lo JH, von Maltzahn G, Douglass J, Park J-H, Sailor MJ, Ruoslahti E, et al. Nanoparticle amplification via photothermal unveiling of cryptic collagen binding sites. J Mater Chem B. 2013; 1: 5235-40.
21. Sapareto SA, Dewey WC. Thermal dose determination in cancer therapy. Int J Radiat Oncol Biol Phys. 1984; 10: 787-800.
22. Chamming's F, Latorre-Ossa H, Le Frère-Belda MA, Fitoussi V, Quibel T, Assayag F, et al. Shear wave elastography of tumour growth in a human breast cancer model with pathological correlation. Eur Radiol. 2013; 23: 2079-86.
23. Lee SH, Moon WK, Cho N, Chang JM, Moon H-G, Han W, et al. Shear-Wave Elastographic Features of Breast Cancers: Comparison With Mechanical Elasticity and Histopathologic Characteristics. Invest Radiol. 2014; 49: 147-55.
24. Athanasiou A, Latorre-Ossa H, Criton A, Tardivon A, Gennisson JL, Tanter M. Feasibility of Imaging and Treatment Monitoring of Breast Lesions with Three-Dimensional Shear Wave Elastography. Ultraschall in Med. 2015; doi: 10.1055/s-0034-1398980.
25. Mariani A, Kwiecinski W, Pernot M, Balvay D, Tanter M, Clement O, et al. Real time shear waves elastography monitoring of thermal ablation: in vivo evaluation in pig livers. J Surg Res. 2014; 188: 37-43.
26. Kwiecinski W, Bessière F, Constanciel E, N'Djin WA, Tanter M, Lafon C, et al. Cardiac shear-wave elastography using a transesophageal transducer: application to the mapping of thermal lesions in ultrasound transesophageal cardiac ablation. Phys Med Biol. 2015; 60: 7829-46.
27. Sapin-de Brosses E, Gennisson JL, Pernot M, Fink M, Tanter M. Temperature dependence of the shear modulus of soft tissues assessed by ultrasound. Phys Med Biol. 2010; 55: 1701-18.
28. Sapin-de Brosses E, Pernot M, Tanter M. The link between tissue elasticity and thermal dose in vivo. Phys Med Biol. 2011; 56: 7755-65.
29. Brown E, McKee T, diTomaso E, Pluen A, Seed B, Boucher Y, et al. Dynamic imaging of collagen and its modulation in tumors in vivo using second-harmonic generation. Nat Med. 2003; 9: 796-800.
30. Shanmugam V, Selvakumar S, Yeh C-S. Near-infrared light-responsive nanomaterials in cancer therapeutics. Chem Soc Rev. 2014; 43: 6254-87.
31. Melamed JR, Edelstein RS, Day ES. Elucidating the Fundamental Mechanisms of Cell Death Triggered by Photothermal Therapy. ACS Nano. 2015; 9: 6-11.
32. Pérez-Hernández M, del Pino P, Mitchell SG, Moros M, Stepien G, Pelaz B, et al. Dissecting the Molecular Mechanism of Apoptosis during Photothermal Therapy Using Gold Nanoprisms. ACS Nano. 2015; 9: 52-61.
33. Marangon I, Ménard-Moyon C, Silva AKA, Bianco A, Luciani N, Gazeau F. Synergic mechanisms of photothermal and photodynamic therapies mediated by photosensitizer/carbon nanotube complexes. Carbon. 2016; 97: 110-23.
34. Miao L, Lin CM, Huang L. Stromal barriers and strategies for the delivery of nanomedicine to desmoplastic tumors. J Control Release. 2015; 219: 192-204.

35. Jain RK, Stylianopoulos T. Delivering nanomedicine to solid tumors. Nat Rev Clin Oncol. 2010; 7: 653-64.
36. Khawar IA, Kim JH, Kuh H-J. Improving drug delivery to solid tumors: Priming the tumor microenvironment. J Control Release. 2015; 201: 78-89.
37. Liang H, Li X, Chen B, Wang B, Zhao Y, Zhuang Y, et al. A collagen-binding EGFR single-chain Fv antibody fragment for the targeted cancer therapy. J Control Release. 2015; 209: 101-9.
38. Wu T, Felmlee J, Greenleaf JF, Riederer SJ, Ehman RL. Assessment of thermal tissue ablation with MR elastography. Magn Reson Med. 2001; 45: 80-7.
39. Chen J, Woodrum DA, Glaser KJ, Murphy MC, Gorny K, Ehman R. Assessment of in vivo Laser Ablation Using MR Elastography with an Inertial Driver. Magn Reson Med. 2014; 72: 59-67.
40. Yarmolenko PS, Moon EJ, Landon C, Manzoor A, Hochman DW, Viglianti BL, et al. Thresholds for thermal damage to normal tissues: An update. Int J Hyperther. 2011; 27: 320-43.
41. Marangon I, Ménard-Moyon C, Kolosnjaj-Tabi J, Béoutis ML, Lartigue L, Alloyeau D, et al. Covalent Functionalization of Multi-walled Carbon Nanotubes with a Gadolinium Chelate for Efficient T1-Weighted Magnetic Resonance Imaging. Adv Funct Mater. 2014; 24: 7173-86.